An efficient and robust method for lithium-ion battery capacity estimation using constant-voltage charging time

Jufeng Yang [a], Xin Li [b,c], Xiaodong Sun [a], Yingfeng Cai [a], Chris Mi [d,*]

[a] Automotive Engineering Research Institute, Jiangsu University, 301 Xuefu Road, Zhenjiang, Jiangsu, 212013, China
[b] School of Electrical Engineering, Southeast University, Nanjing, 210096, China
[c] School of Electrical and Electronic Engineering, Nanyang Technological University, 639798, Singapore
[d] Department of Electrical and Computer Engineering, San Diego State University, 5500 Campanile Drive, San Diego, CA, 92182, USA

A R T I C L E   I N F O

A B S T R A C T

The state-of-health (SoH) estimation based on the constant-voltage (CV) charging data has been an interesting research topic in recent years. However, most of the existing estimation methods based on CV charging data are sensitive to the cut-off condition and/or require a relatively high storage resource as well as computing power, preventing the feasibility in real world applications. To extend the scope of the estimation method based on CV charging data, this paper proposes a quick and robust battery capacity estimation method using a two-layer CV charging time (T_{CV})-based model. First, the evolution of T_{CV}-based SoH model with respect to different cut-off currents is investigated, and the detailed mathematical expressions of the model coefficients are derived based on the decoupled dynamic characteristics of the CV charging current. Second, considering the actual sampling periods (T_ss) utilized in the online application, a T_s-adaptive moving average filter is proposed to filter the high-frequency measurement noise. Third, experimental results demonstrate that the proposed method can determine SoH with a root-mean-square error of less than 2.05% for two types of tested batteries under different charging protocols. In addition, the comparison study further highlights the superiority of the proposed method in terms of robustness, accuracy, computational cost, and storage consumption.

1. Introduction

Lithium-ion batteries have become a promising battery technology due to the advantages of high energy density, high power, and relatively long cycle life [1,2]. They have been extensively used, ranging from low power consumer electronics [3,4], to high power traction applications [5,6]. For example, in traction applications like electric vehicles (EVs), lithium-ion batteries are widely used as the energy storage system in battery powered or hybrid electric vehicles to help reduce gas emission and fossil fuel consumption. The battery capacity is one of the core parameters to evaluate the battery performance. The actual capacity degrades as the battery cycles, which influences the driving range of the vehicle, and further increases the "range anxiety" [7]. Therefore, it is essential to monitor the battery state-of-health (SoH) related to the energy capability in real-time for the safe and reliable battery utilization [8,9].

1.1. Literature review

Extensive research efforts have been focused on the estimation of battery SoH in recent years, which can be roughly categorized into discharging data-based and charging data-based methods in terms of the working conditions.

The discharging data-based methods can be further divided into indirect estimation and direct identification methods. For the first type, the model parameters and the battery capacity or other aging-sensitive parameters are generally combined into a state vector, and identified through a series of adaptive algorithms, such as least squares estimation-based [10], filter-based [11], and observer-based techniques [12]. It should be noted that the performance of the adaptive algorithm strongly depends on the employed model structure and the algorithm parameters. As for the second type, the vehicle driving data (current, voltage, and temperature) recorded by the battery management system (BMS) are directly used or investigated to extract the feature-of-interests (FoIs) reflecting the battery capacity degradation. Then, considering these variables as input features, some machine learning techniques, such as

---

* Corresponding author.
  E-mail addresses: yjf@ujs.edu.cn (J. Yang), cmi@sdsu.edu (C. Mi).

Nomenclature

a_i, i = 1-3	Parameters of SoH model
b_i, i = 1-5	Parameters of SoH model
B	Intercept of linear function
Cap	Battery capacity [Ah]
Cap_{est}	Estimated battery capacity [Ah]
Cap_{nom}	Nominal battery capacity [Ah]
E_{CV}	Energy of constant-voltage charging process
$f(\bullet)$	Parameter function
f	Frequency of input signal [Hz]
f_{cut}	Cut-off frequency [Hz]
I_{CC}	Constant-current charging current [A]
I_{cut}	Cut-off current [A]
I_{mea}	Measured current [A]
I_{avg}	Filtered current [A]
I_{low}	Lower limit of current range [A]
I_{up}	Upper limit of current range [A]
I_1	Fast-dynamic current [A]
I_2	Slow-dynamic current [A]
K	Slope of linear function
k_i, i = 1-4	Parameters of SoH model
N_d	Total number of data points
N_b	Buffer length
r	Correlation coefficient
R^2	R-square
T_{CV}	Constant-voltage charging time [s]
T_s	Sampling period [s]
T_w	Window length
t	Time [s]
t_{end}	Time instant at the end of the constant-voltage charging process [s]
t_{FoI}	Computational cost of feature-of-interest extraction [s]
t_{model}	Computational cost of offline model construction [s]
t_0	Time instant at the beginning of the constant-voltage charging process [s]
V_{low}	Lower limit of voltage range [V]
V_{up}	Upper limit of voltage range [V]
V_t	Battery terminal voltage [V]
x	Independent variable
$\bar{x}$	Mean value of independent variable
y	Observation variable
$\bar{y}$	Mean value of observation variable
τ_{CV}	Time constant of the decoupled constant-voltage charging current [s]
τ_1	Fast-dynamic time constant [s]
τ_2	Slow-dynamic time constant [s]

Subscripts

aged	aged state
avg	filtered
cut	cut-off
est	estimated
mea	measured
new	new state
nom	nominal
on	online
off	offline

Greek symbols

Δ	A change in the value
τ	Time constant [s]
ω	Radian frequency [Hz]

Acronyms

BMS	Battery management system
CC	Constant-current
CV	Constant-voltage
DTV	Differential thermal voltammetry
DVA	Differential voltage analysis
EV	Electric vehicle
FNN	Feedforward Neural network
FoI	Feature-of-interest
ICA	Incremental capacity analysis
LFP	Lithium iron phosphate
MAF	Moving average filter
NCA	Nickel cobalt aluminum oxide
PA	Peak area
RMSE	Root mean-square error
SoH	State-of-health

support vector machine, Gaussian process regression, relevance vector machine, and so on, can be utilized to train an SoH model [13–15]. Generally, more computational cost is required with the increasing number of input features. With the development of cloud computing in recent years, this kind of methods has great potential to be implemented in EV applications [16].

Unlike the dynamic and random discharging scenario, the charging scenario is relatively simple, stable, and predictable, thus the charging data have been widely adopted for the battery SoH estimation. One of the commonly used charging data-based methods is differential analysis technique, which mainly includes incremental capacity analysis (ICA) [17,18], differential voltage analysis (DVA) [19,20], and differential thermal voltammetry (DTV) [21,22]. Through the differential operation, the plateaus regions on the measured terminal voltage or the surface temperature curve under the long-term constant-current (CC) charging scenario can be transformed to the identifiable peak/valleys on the differential curve. It has been proved that the height, area, and location of the relevant peak/valleys are effective FoIs, and can be employed to establish the SoH estimation model [16]. However, two main disadvantages exist concerning the differential analysis methods. Firstly, this kind of methods is sensitive to the current rates. For example, to reduce the influence of the polarization effect, ICA/DVA

methods are usually implemented at the moderate or even low current rates [16,23]. While for the DTV method, a higher current rate is preferred to guarantee observable heat generation. Secondly, the long-term CC charging process is required to obtain the comprehensive peak/valley information. Nevertheless, in practical applications like EVs, the discharging process is strongly dependent on the driving habits and battery is rarely fully discharged, which subsequently influences the initial charging state. In addition, to reduce the charging time and improve the energy transfer efficiency, multistage CC charging protocol, which contains multiple short-term CC charging processes with different current rates, has been widely used in EVs. Under the above working conditions, FoIs cannot be effectively extracted by the differential analysis method. To overcome these limitations, Ref. [24] proposed a deep-learning approach to estimate the entire CC charging curves only based on the small portions of the charging data, and thus the battery capacity can be extracted under the incomplete charging scenario. In order to reduce the influence of current rate on the ICA, Ref. [25] proposed a robust battery SoH prediction method to correct the peak shift through polarization compensation. With respect to the fast charging scenario, Refs. [26,27] investigated the evolution of battery terminal voltage under multistage CC charging scenario, and extracted several FoIs from the partial charging curve to correlate with the battery
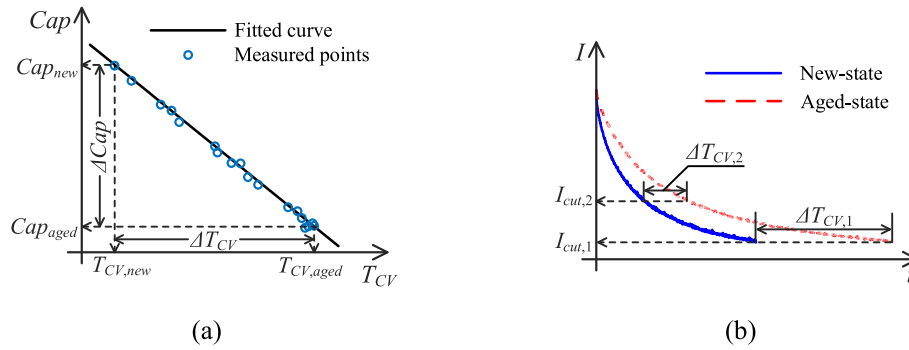
Fig. 1. Schematic representation of (a) *Cap* versus T_{CV} for a certain I_{cut}; (b) CV charging currents at different aging states (exemplarily with the measurements from the tested LFP battery).

capacity degradation. In addition, Ref. [28] introduced the battery terminal voltage at 80% SoC for about 10 min as the FoI, and proposed a long short-term memory-fully connected network to deal with battery inconsistency caused by fast charging.

It has been found that the constant-voltage (CV) charging protocol applied after the CC charging process can effectively reduce the electrode polarization and slow down the battery degradation rate [29,30]. In addition, compared to the CC charging process, the CV charging process is more robust to the preceding discharging process and flexible with the initial charging state. Hence, identifying the battery SoH based on CV charging data has been an interesting topic and has attracted wide attention in recent year. The relevant research work has revealed that the charging time [31–33], the capacity [34], the time constant [35,36], and the energy [37,38] extracted based on the CV charging data are effective FoIs to characterize the battery aging state. Among them, the CV charging time (T_{CV}) is a simple and direct FoI because it can be obtained as soon as the CV charging process is complete, and no sophisticated parameter identification procedure is required. However, T_{CV} is sensitive to the cut-off condition. The random and uncertain factors in practical application may compromise the estimation performance. Besides, due to the gradually decreasing current, the CV charging process is time-consuming, especially when the charging current is below a certain value. Hence, some charging strategies perform the CV charging process for a certain duration [39], where the conventional T_{CV}-based SoH estimation method cannot work. Considering the partial CV charging process, the indirect FoIs are generally extracted to estimate the battery SoH. For example, Ref. [35] employed the current time constant as the input of the established SoH estimation model, and developed a logarithmic function-based prediction model to estimate the reference current time constant. In addition, Ref. [34] selected the CV capacity as the FoI, and iteratively incorporated the Q-V modeling with the open-circuit voltage estimation to reconstruct the complete CV phase. The verification results demonstrated the satisfactory SoH estimation performance even under the partial CV charging scenario. It should be noted that for the indirect FoI-based SoH estimation method, the charging data during the CV process should be recorded to identify the model parameters, at the expense of high storage consumption, especially for the battery system with the long-time CV charging process and/or high sampling frequency. Besides, the parameter identification procedure consumes the computing power of the on-board microcontroller.

1.2. Motivations and contributions

It can be concluded from the previous study that the existing CV charging data-based SoH estimation methods using indirect FoIs generally suffer from high storage resource and computing power. While for the direct FoI-based method, two main challenges are summarized as follows:

(1) **Sensitive to the cut-off condition:** the conventional T_{CV}-based SoH model is established under a specific cut-off condition, i.e., the constant cut-off current (I_{cut}). This limits the utilization of this method in real-world applications with random and uncertain I_{cut}s.

(2) **Limited to the constant sampling period:** in the existing study, the sampling periods in the offline identification and online estimation procedures are generally considered as the same value. However, to save memory space for the on-board BMS, a flexible sampling frequency is recently introduced in real world applications [40]. This may reduce the generalization capability of the established SoH model.

Hence, there is still room to improve the CV charging data-based method, in terms of simultaneously reducing complexity and improving robustness. To bridge the aforementioned research gap, a robust and computationally efficient T_{CV}-based SoH estimation method is proposed in this paper. The main contributions are summarized as:

(1) **Established a two-layer T_{CV}-based SoH model insensitive to the cut-off condition:** the evolution of the correlation between the battery capacity and T_{CV} with respect to different I_{cut}s is investigated. Subsequently, based on a second-order exponential model developed in our previous work [41], the coefficients of the T_{CV}-SoH correlation are mathematically characterized as functions of I_{cut}.

(2) **Proposed a sampling period-adaptive filter:** the influence of the window length on the performance of a moving average filter (MAF) is discussed in the continuous-time domain. Then, based on the sampling periods utilized in the offline test and the online application, an adjustment method of the reserved buffer length is proposed to realize a sampling period-adaptive MAF.

(3) **Validated the effectiveness under different charging conditions:** based on two battery degradation datasets, the estimation performance is systematically evaluated under different CV charging scenarios, including the constant I_{cut} cut-off condition, the constant T_{CV} cut-off condition, and the different sampling periods. In addition, the conventional T_{CV}-based and some other state-of-art estimation methods are employed to conduct a comparative study.

2. Model establishment

2.1. Model evolution

Based on the existing research [32,42], due to the increased resistance and the decreased diffusion at the electrode/electrolyte interface, T_{CV} generally increases with the degrading battery capacity (*Cap*) for a certain I_{cut}, as schematically shown in Fig. 1(a), where the measured
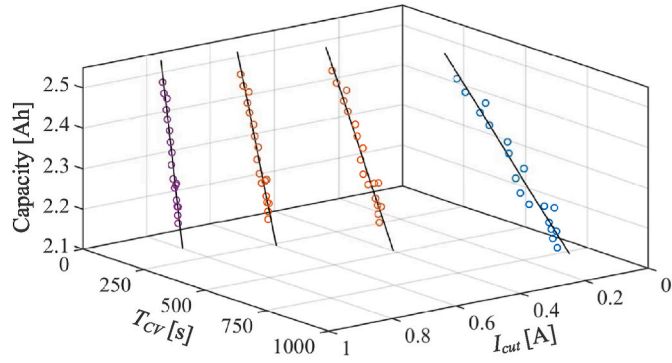
Fig. 2. Correlations between *Cap* and T_{CV} at different I_{cut}s (exemplarily with the test data from the adopted LFP battery).

points are extracted from the test data of the employed lithium iron phosphate (LFP) battery. Considering the tendency of the related data, the linear function expressed as (1) is employed to describe the relationship between *Cap* and T_{CV}, where Cap_{est} denotes the estimated battery capacity, K and B denote the slope and the intercept of the linear function, respectively.

$$Cap_{est} = KT_{CV} + B \tag{1}$$

As shown in Fig. 1(a), K can be further expressed as

$$K = \frac{\Delta Cap}{\Delta T_{CV}} = \frac{Cap_{aged} - Cap_{new}}{T_{CV,aged} - T_{CV,new}} \tag{2}$$

where ΔCap and ΔT_{CV} denote the change of *Cap* and T_{CV} respectively, Cap_{new} and Cap_{aged} denote the battery capacity in the new and aged states, respectively, $T_{CV,new}$ and $T_{CV,aged}$ denote T_{CV} corresponding to the new-state and aged-state batteries, respectively.

It is evident from (2) that for a certain ΔCap, the value of K depends on ΔT_{CV}. The battery CV charging current curves at different aging states are schematically presented in Fig. 1(b). It can be observed that in a certain aging state, there exists a specific one-to-one mapping correlation between the CV charging current and the time instant, thus ΔT_{CV} can be expressed as a variable with respect to I_{cut}, i.e.,

$$\Delta T_{CV} = T_{CV,aged} - T_{CV,new} = f_{T_{CV,aged}}(I_{cut}) - f_{T_{CV,new}}(I_{cut}) = f_{\Delta T_{CV}}(I_{cut}) \tag{3}$$

where $f_{T_{CV,new}}(I_{cut})$, $f_{T_{CV,aged}}(I_{cut})$, and $f_{\Delta T_{CV}}(I_{cut})$ denote the functions mapping I_{cut} to $T_{CV,new}$, $T_{CV,aged}$, and ΔT_{CV}, respectively.

It can be concluded from (1) to (3) that the coefficients of the correlation between *Cap* and T_{CV} demonstrate diverse values with respect to different I_{cut}s, as exemplarily illustrated in Fig. 2.

Therefore, Eq. (1) can be further expressed as

$$Cap_{est} = f_K(I_{cut})T_{CV} + f_B(I_{cut}) \tag{4}$$

where $f_K(I_{cut})$ and $f_B(I_{cut})$ denote the functions mapping I_{cut} to K and B in (1), respectively.

Hence, in order to extend the scope of the T_{CV}-based SoH estimation method and improve the robustness of this method under different CV charging conditions, the correlations between *Cap* and T_{CV} corresponding to different I_{cut}s are required to be established in advance.
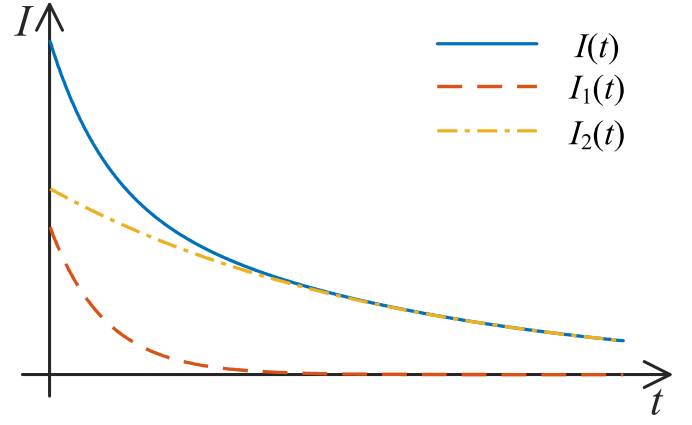

Fig. 3. Schematic representation of CV charging current and decoupled components.

2.2. Mathematical expression of model

According to the aforementioned analysis, the evolution of K with respect to I_{cut} is closely related to the change of ΔT_{CV} with I_{cut}. Hence, it is critical to establish the correlation between ΔT_{CV} and I_{cut}. Based on our previous work, the charging current under CV scenario can be quantitatively expressed as the sum of two current components with different scales of time constants [41], i.e.,

$$I(t) = I_1(t) + I_2(t) = I_1(0)e^{-\frac{t}{\tau_1}} + I_2(0)e^{-\frac{t}{\tau_2}} \tag{5}$$

where t denotes the CV charging time, and $t = 0$ denotes the start of the CV charging process, $I_1(t)$ and $I_2(t)$ denote the fast-dynamic and the slow-dynamic currents, respectively, τ_1 and τ_2 denote the time constants corresponding to $I_1(t)$ and $I_2(t)$, respectively, and $\tau_1 < \tau_2$.

The evolution of $I(t)$, $I_1(t)$ and $I_2(t)$ are schematically shown in Fig. 3.

It can be seen from Fig. 3 that at the end of the CV charging process, $I_1(t)$ has converged to zero due to the fast-dynamic characteristic, and $I(t)$ at this stage mainly contains $I_2(t)$, as

$$I(t) = I_2(0)e^{-\frac{t}{\tau_2}} \tag{6}$$

Therefore, T_{CV} is mainly determined by the slow-dynamic current component. Based on (6), the expression of T_{CV} with respect to I_{cut} is

$$T_{CV} = -\tau_2 \ln[I_{cut}/I_2(0)] \tag{7}$$

Specifically, τ_2 and $I_2(0)$ can be obtained based on the nonlinear least squares method, and the identified parameters are closely related to the predefined I_{cut}, which is equivalent to the size of the dataset. The evolution of identified τ_2 and $I_2(0)$ corresponding to different I_{cut}s is exemplarily shown in Fig. 4. The fitted linear regression functions are also presented in the figure for a quantitative comparison.

It can be observed from Fig. 4 that both τ_2 and $I_2(0)$ demonstrate strong dependencies with I_{cut}. In addition, the change magnitude of $I_2(0)$ is far more less than the change magnitude of τ_2, thus the value of $I_2(0)$ can be approximately regarded as constant. Therefore, τ_2 and $I_2(0)$ can be further expressed as $\tau_2 = a_1 I_{cut} + a_2$ and $I_2(0) \approx a_3$, respectively.

Based on the aforementioned analysis, the detailed expression of ΔT_{CV} with respect to I_{cut} is

$$\Delta T_{CV} = T_{CV,aged} - T_{CV,new} - \tau_{2,aged}\ln[I_{cut}/I_{2,aged}(0)] + \tau_{2,new}\ln[I_{cut}/I_{2,new}(0)] = (-\tau_{2,aged} + \tau_{2,new})\ln(I_{cut}) + \tau_{2,aged}\ln[I_{2,aged}(0)] - \tau_{2,new}\ln[I_{2,new}(0)]$$
$$= (k_1 I_{cut} + k_2)\ln(I_{cut}) + k_3 I_{cut} + k_4 = f_{\Delta T_{CV}}(I_{cut}) \tag{8}$$
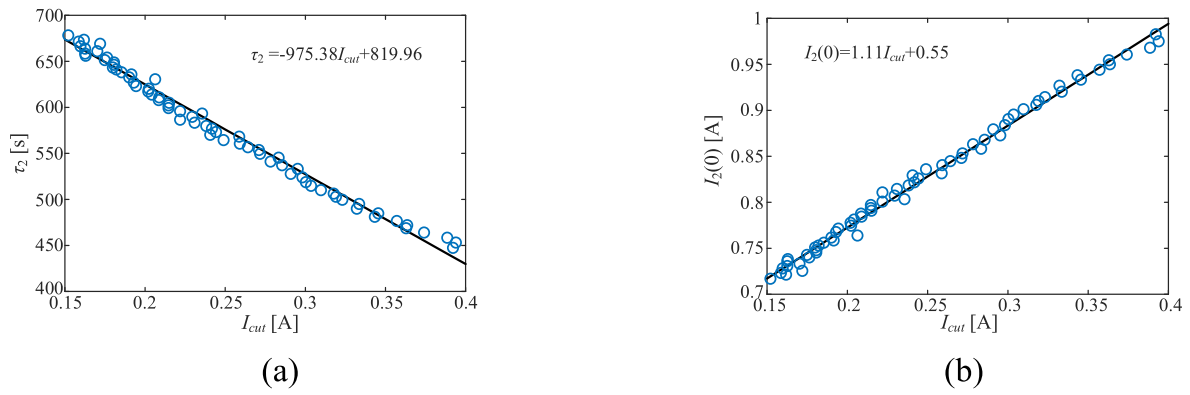
Fig. 4. Evolution of (a) τ_2 and (b) $I_2(0)$ with respect to I_{cut} (exemplarily with the test data from the adopted LFP battery).

where $\tau_{2,new}$ and $\tau_{2,aged}$ denote τ_2 for the new-state and aged-state batteries, respectively, $I_{2,new}(0)$ and $I_{2,aged}(0)$ denote $I_2(0)$ for the new-state and aged-state batteries, respectively, k_1, k_2, k_3, and k_4 denote the function coefficients required to be identified. The above parameters satisfy

$$\tau_{2,new} = a_{1,new}I_{cut} + a_{2,new}$$
$$\tau_{2,aged} = a_{1,aged}I_{cut} + a_{2,aged}$$
$$I_{2,new}(0) = a_{3,new}$$
$$I_{2,aged}(0) = a_{3,aged}$$
$$k_1 = -a_{1,aged} + a_{1,new}$$
$$k_2 = -a_{2,aged} + a_{2,new}$$
$$k_3 = a_{1,aged}\ln(a_{3,aged}) - a_{1,new}\ln(a_{3,new})$$
$$k_4 = a_{2,aged}\ln(a_{3,aged}) - a_{2,new}\ln(a_{3,new})$$

In addition, for a certain *Cap*, *B* in (1) can be further expressed as a function of I_{cut}, i.e.,

$$b_1 = Cap$$
$$b_2 = -a_1\Delta Cap$$
$$b_3 = -a_2\Delta Cap$$
$$b_4 = a_1\Delta Cap \ln(a_3)$$
$$b_5 = a_2\Delta Cap \ln(a_3)$$

It can be concluded that with the knowledge of I_{cut}, the correlation between *Cap* and T_{CV} can be obtained online by using the established function expressed as (8) and (9). Subsequently, the actual battery capacity can be identified by substituting T_{CV} into the obtained correlation.

3. Sampling period-adaptive moving average filter (MAF)

In order to reduce the influence of the high-frequency measurement noise on the current measurement, the moving average filter (MAF) is utilized in this study due to the advantages of simple realization and low

$$B = Cap - \left[\Delta Cap \big/ f_{\Delta T_{CV}}(I_{cut})\right]\left\{-\tau_2 \ln[I_{cut}/I_2(0)]\right\} = Cap - \left[\Delta Cap \big/ f_{\Delta T_{CV}}(I_{cut})\right]\left[-(a_1 I_{cut} + a_2)\ln(I_{cut}) + (a_1 I_{cut} + a_2)\ln(a_3)\right]$$
$$= b_1 - \left[(b_2 I_{cut} + b_3)\ln(I_{cut}) + b_4 I_{cut} + b_5\right] \big/ f_{\Delta T_{CV}}(I_{cut}) = f_B(I_{cut}) \tag{9}$$

where b_1, b_2, b_3, b_4, and b_5 are function coefficients required to be identified, and satisfy

computational cost [43].

3.2. Characteristic analysis of MAF

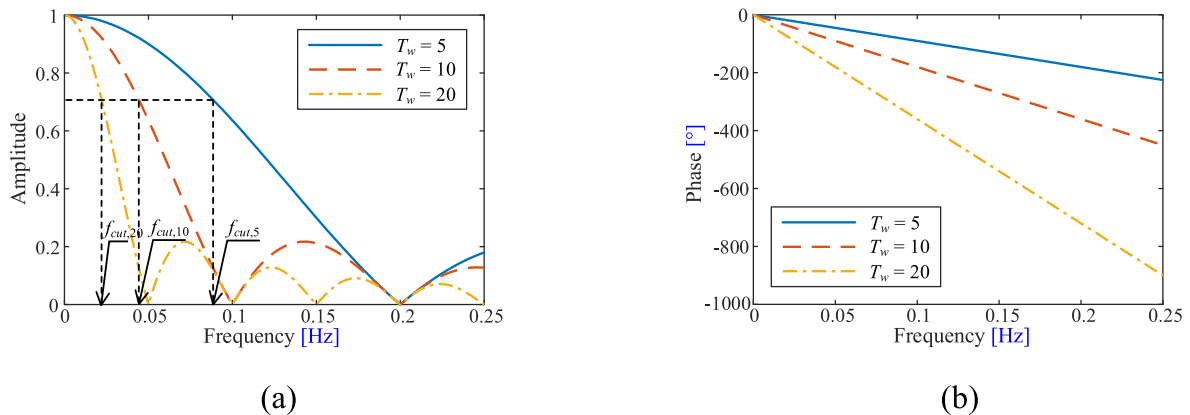The MAF calculates the output by averaging a series of input data

Fig. 5. (a) Magnitude and (b) phase responses of MAF with respect to frequency.
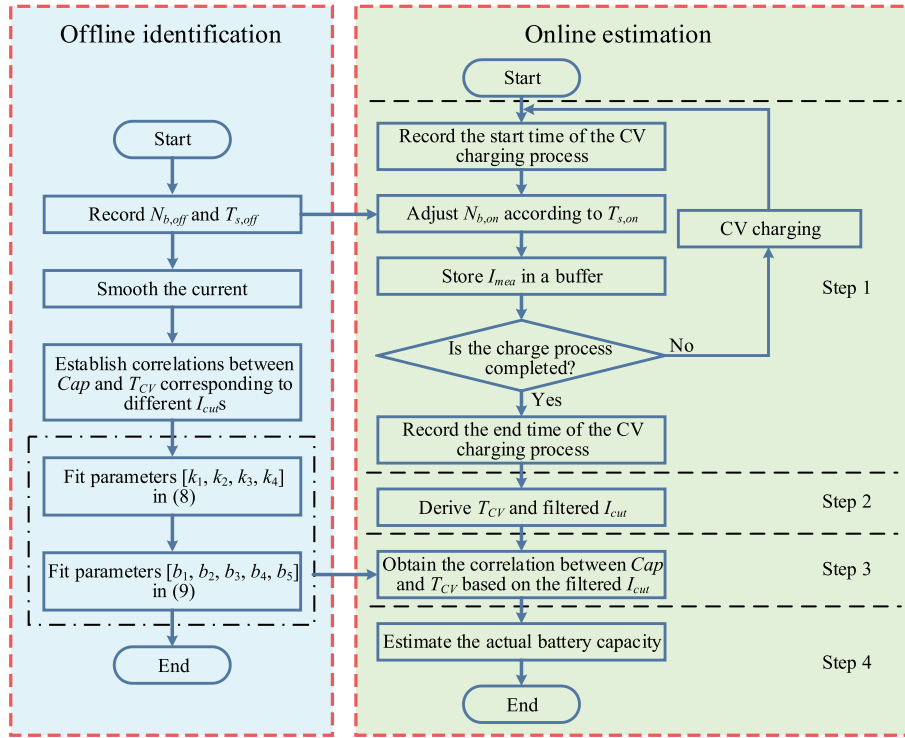
Fig. 6. Proposed battery capacity estimation scheme.

within a certain window length (T_w), and the relevant expression in continuous-time domain is [44].

$$I_{avg}(t) = \frac{1}{T_w} \int_{t-T_w}^{t} I_{mea}(\tau)d\tau \qquad (10)$$

where I_{mea} and I_{avg} denote the measured and the filtered current, respectively.

Based on (10), Eq. (11) can be obtained after the Laplace transformation.

$$I_{avg}(s) = \left(1 - e^{-sT_w}\right)I_{mea}(s) \big/ T_w s \qquad (11)$$

Substituting $s = j\omega$ into (11), the transfer function of MAF (H_{MAF}) is

$$H_{MAF}(j\omega) = \frac{I_{avg}(j\omega)}{I_{mea}(j\omega)} = \frac{1 - e^{-jT_w\omega}}{jT_w\omega} = \left|\frac{\sin(\omega T_w/2)}{\omega T_w/2}\right|e^{-j\omega T_w/2} = \left|\frac{\sin(\pi f T_w)}{\pi f T_w}\right|e^{-j\pi f T_w} \qquad (12)$$

where ω and f denote the radian frequency and the frequency of the input signal, respectively, and $\omega = 2\pi f$.

The magnitude and phase responses of MAF with different T_ws are shown in Fig. 5, and the corresponding cut-off frequencies (f_{cut}s) are marked in Fig. 5(a). As can be seen, the high-frequency components are overall attenuated by the MAF, which is similar to the characteristic of an ideal low-pass filter. Besides, f_{cut} monotonically reduces as T_w increases, which will lead to more amplitude attenuation and larger phase lag for the filter output. Hence, the characteristic of the MAF output is closely related to the value of T_w.

3.2. Discrete-time realization

Based on (10), the discrete-time expression of MAF is [44].

$$I_{avg}(t) = \frac{1}{N_b} \sum_{k=0}^{N_b-1} I_{mea}(t - kT_s) \qquad (13)$$

where T_s denotes the sampling period, N_b denotes the length of the

buffer to store I_{mea}, and $T_w = N_b T_s$. Specifically, the "first-in, first-out" method is utilized to manipulate the current measurements, and the filter algorithm is only conducted at the end of the CV charging process.

According to the aforementioned analysis, the performance of the MAF is mainly influenced by T_w, which is dependent on N_b and T_s. In the practical BMS, considering the storage and computation capabilities of the employed microcontroller, T_s may be different from that utilized in the offline test [26,40]. If N_b in (13) is not adjusted according to the actual T_s, the trajectory of the filtered current will demonstrate different dynamic characteristics even in the same aging state, which will deteriorate the battery capacity estimation accuracy. Therefore, to ensure the generality of the established correlation, the actual buffer length in the practical application ($N_{b,on}$) should yield to

$$T_{w,on} = T_{w,off} \quad \Rightarrow \quad N_{b,on} = N_{b,off}\left(T_{s,off} \big/ T_{s,on}\right) \qquad (14)$$

where $N_{b,off}$ is the buffer length utilized in the offline correlation establishment procedure, $T_{w,off}$ and $T_{w,on}$ denote the window lengths used in the offline and online procedures, respectively, $T_{s,off}$ and $T_{s,on}$ denote the offline and online sampling period, respectively.

4. Framework of the proposed method

The scheme of the proposed battery capacity estimation method is shown in Fig. 6. It mainly includes two parts, i.e., offline identification and online estimation.

The offline identification process is conducted based on the test data of the selected reference battery, and it mainly consists of two layers. In the first layer, the CV charging current is smoothed using the MAF, and the employed $N_{b,off}$ as well as $T_{s,off}$ are recorded for the online estimation. Then, for a specific current range [I_{low}, I_{up}], the correlations between Cap and T_{CV} corresponding to different I_{cut}s are fitted at a certain current interval ΔI, i.e., K and B in (1) corresponding to $I_{low} + k\Delta I$ [$k = 0$, 1, 2, ..., (I_{up}-I_{low})/ΔI] are obtained. In the second layer, k_1-k_4 in (8) are identified by fitting the relationship between $1/K$ and I_{cut}, then b_1-b_5 in (9) are further determined by fitting the relationship between B and I_{cut}. Lastly, the obtained k_1-k_4 and b_1-b_5 are stored in the on-board

Table 1

Battery test procedures.

Procedure	LFP	NCA
1 Cycling tests		
1.1 Charge process	CC charge at 1 C-rate	CCCV charge at 0.5 C-rate
1.2 Rest process	0 min	30 min
1.3 Discharge process	CC discharge at 4 C-rate	CC discharge at 0.5 C-rate
1.4 Rest process	0 min	60 min
2 Characterization tests		
2.1 Charge process	CCCV charge at 0.5 C-rate	CCCV charge at 0.5 C-rate
2.2 Rest process	60 min	30 min
2.3 Discharge process	CC discharge at 1 C-rate	CC discharge at 0.5 C-rate
2.4 Rest process	60 min	60 min

microcontroller for the online estimation.

The online estimation process can be summarized as four steps. In step 1, the time instants at the beginning (t_0) and the end (t_{end}) of the CV charging process are recorded. Besides, according to $T_{s,on}$, $N_{b,on}$ is adjusted based on (14), and the measured current is stored in a buffer during the CV charging process. In step 2, the recorded data is pre-processed when the CV charging process is finished. T_{CV} is derived by subtracting t_0 from t_{end}, i.e., $T_{CV} = t_{end}\text{-}t_0$. Meanwhile, the filtered I_{cut} is obtained by applying the MAF on the data stored in the buffer. In step 3, according to the filtered I_{cut}, the quantitative correlation between *Cap* and T_{CV} can be established by using (8) and (9), which have been determined in the offline identification process. In step 4, the actual battery capacity can be obtained by substituting T_{CV} into the correlation established in step 3.

5. Experimental validation and discussion

5.1. Experimental setup and test procedure

Two groups of lithium-ion batteries, including four 2.5 Ah LFP batteries (numbered from #1 to #4) and three 4.8Ah nickel cobalt aluminum oxide (NCA) batteries (numbered from #5 to #7), are adopted for the test. Specifically, the batteries in each group are selected with the similar characteristics, thus the influence of the battery inconsistency on the estimation result is not considered in this study

The tests for the LFP batteries are performed by an 8-channel Arbin BT2000 cycle-based tester, and all three NCA batteries are charged/discharged by a 16-channel NBT5V20AC16-T battery cycler. All of the tests are conducted at the temperature around 25 °C, and the test data are recorded with the predefined T_s of 1 s. The test procedures are presented in Table 1.In this study, all single battery results are based on the test data of batteries #1 and #5 for the LFP and the NCA batteries, respectively.

5.2. Analysis of offline identification performance

A. Determination of I_{cut} range

It can be concluded from Section 4 that in the offline identification process, the correlation between *Cap* and T_{CV} should be established in a certain range of I_{cut}, that is, [I_{low}, I_{up}]. Hence, it is critical to determine an appropriate range of I_{cut} according to the dynamic characteristics of the CV charging current at different aging states. The evolution of the CV charging current throughout the aging process is shown in Fig. 7. As can be seen, for LFP battery, the variation rate of the current curve overall decreases as cycle number increases, which means that T_{CV} corresponding to a certain I_{cut} possesses an increasing trend with respect to the degrading capacity. By contrast, for NCA battery, the time for the
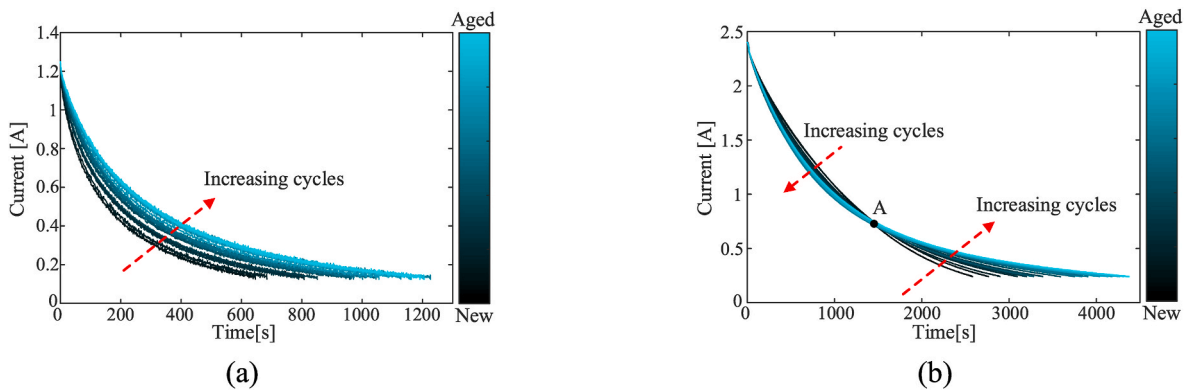
Fig. 7. CV charging current curves for (a) battery #1 and (b) battery #5 after different cycles.
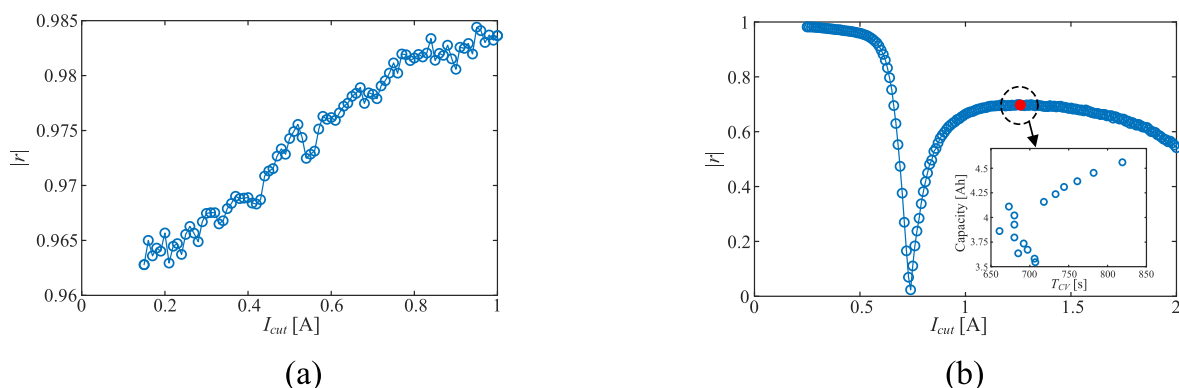
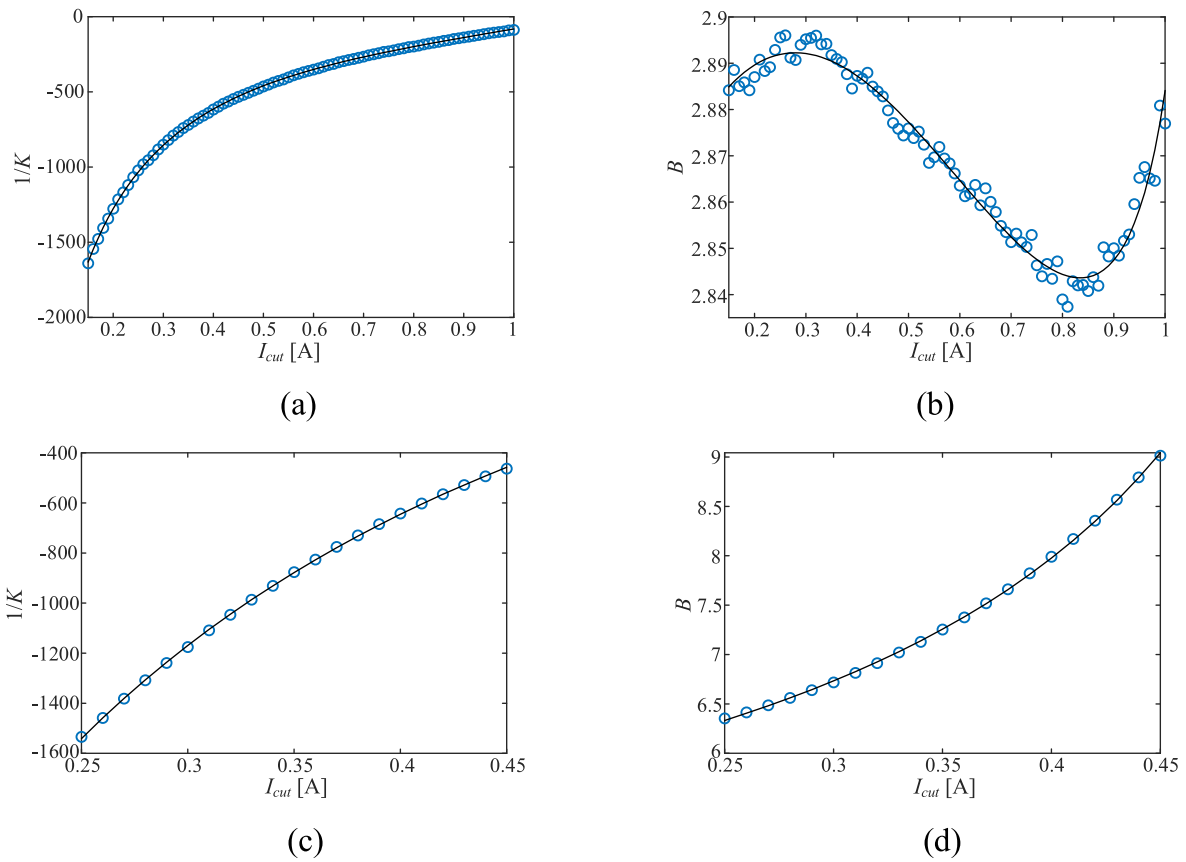**Fig. 8.** Evolution of |r| with respect to I_{cut} for (a) battery #1 and (b) battery #5.

Fig. 9. Evolution of model coefficients with respect to I_{cut}. (a) $1/K$ for battery #1. (b) B for battery #1. (c) $1/K$ for battery #5. (d) B for battery #5.

Table 2
Identified model coefficients.

	LFP	NCA
$[k_1, k_2, k_3, k_4]$	$[2.045 \times 10^3, 2.130 \times 10^3, -3.615 \times 10^3, 3.533 \times 10^3]$	$[9.574 \times 10^{-7}, 2.853 \times 10^3, -2.967 \times 10^3, 3.155 \times 10^3]$
R^2 of fitted $1/K$	0.9999	0.9999
$[b_1, b_2, b_3, b_4, b_5]$	$[2.458 \times 10^2, 2.256 \times 10, -2.387 \times 10^2, 2.434 \times 10^2, 2.827]$	$[1.262 \times 10^{-3}, 1.820 \times 10^3, -4.200 \times 10^3, 5.010 \times 10^3, 5.400]$
R^2 of fitted B	0.9755	0.9998

current to decline to approximately 0.74 A are almost identical at different aging states, as shown the point A in Fig. 7(b), indicating that the corresponding T_{CV} cannot be used to reflect the battery capacity loss.

The correlation coefficient (r) is utilized to further determine the appropriate range of I_{cut}, and r is expressed as [36].

$$r = \frac{\sum\limits_{i=1}^{N_d}(x_i - \overline{x})(y_i - \overline{y})}{\sqrt{\sum\limits_{i=1}^{N_d}(x_i - \overline{x})^2}\sqrt{\sum\limits_{i=1}^{N_d}(y_i - \overline{y})^2}} \tag{15}$$

where x and y represent T_{CV} and the battery capacity, respectively, $\overline{x}$ and $\overline{y}$ denote the mean values of x and y, respectively, N_d denotes the total number of data points for four LFP or three NCA batteries. The evolution of the absolute values of the correlation coefficient ($|r|$) versus I_{cut} is shown in Fig. 8.

As can be seen, $|r|$ for the tested LFP battery is generally larger than 0.95, and the values progressively approaches 1 with the increasing I_{cut}, that is, Cap demonstrates a stronger linear dependency on T_{CV} with higher I_{cut}. For the employed NCA battery, there is a sudden drop of $|r|$ at around 0.74 A, which is consistent with the trend of the current evolution shown in Fig. 7(b). Besides, although the correlation is significantly improved when I_{cut} is larger than 0.74 A, the corresponding $|r|$s are still
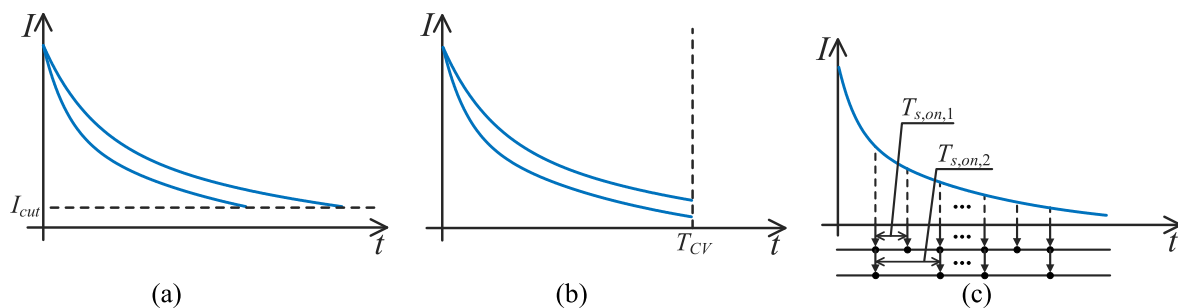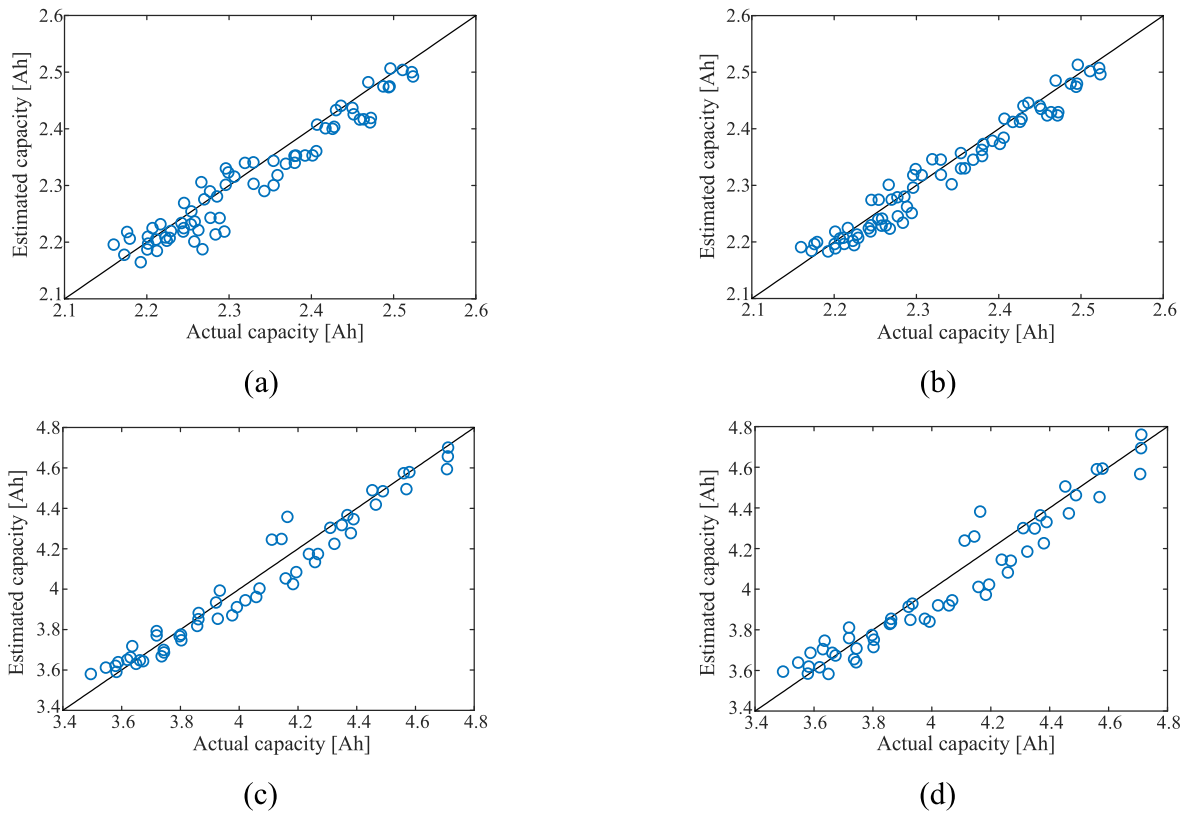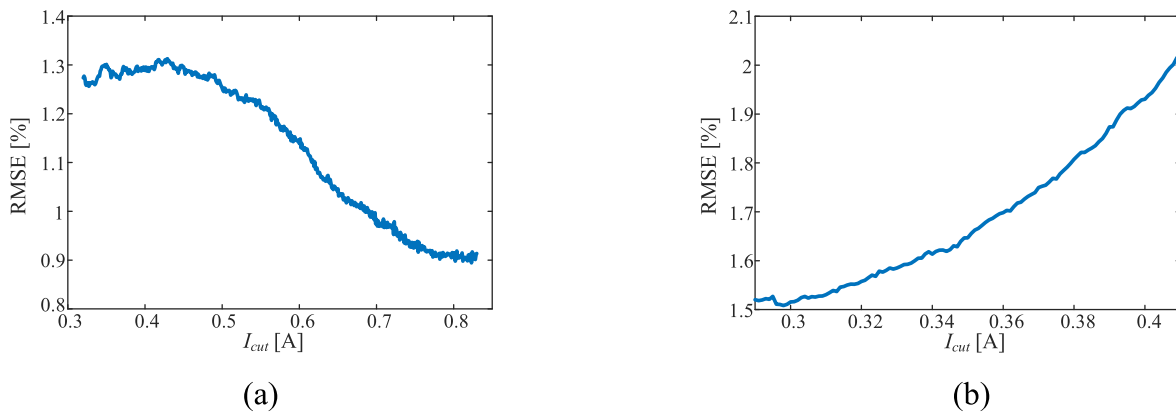

Fig. 10. Schematical representation of three verification cases. (a) Constant I_{cut} cut-off condition. (b) Constant T_{CV} cut-off condition. (c) Different $T_{s,on}$s.

Fig. 11. Estimation results of two batteries with different I_{cut}s. LFP battery with (a) $I_{cut} = 0.32$ A and (b) $I_{cut} = 0.83$ A. NCA battery with (c) $I_{cut} = 0.29$ A and (d) $I_{cut} = 0.41$ A.

Fig. 12. Evolution of RMSE with respect to I_{cut} for (a) LFP and (b) NCA batteries.

less than the values in the lower I_{cut} range. This is because within this I_{cut} range, there is no obvious one-to-one mapping correlation between *Cap* and T_{CV} when *Cap* degrades less than 4 Ah, as shown in the inset of Fig. 8 (b). Based on the above analysis, the ranges of I_{cut} for the tested LFP and NCA batteries are determined as [0.15, 1.0] and [0.25, 0.45] A, respectively.

B. Fitting results of model coefficients.

According to the determined [I_{low}, I_{up}], the relationships between I_{cut} and $1/K$ as well as *B* for two types of batteries are depicted in Fig. 9, where the solid lines represent the fitted $f_{1/K}(I_{cut})$ and $f_B(I_{cut})$. The fitted function coefficients are listed in Table 2, and the values of R-square (R^2) are also listed in the table to measure the fitting accuracy. It can be concluded from Fig. 9 and Table 2 that the adopted fitting functions can accurately describe the variation trends of $1/K$ and *B*.

### 5.3. Analysis of online estimation performance

In order to validate the effectiveness and robustness of the proposed method, three cases, that is, constant I_{cut} cut-off condition, constant T_{CV} cut-off condition, and different $T_{s,on}$s, as illustrated in Fig. 10, are considered in this section.

A. Case 1: constant I_{cut} cut-off condition

In order to evaluate the estimation performance, the scatter plots of Cap_{est} versus *Cap* with different I_{cut}s are demonstrated in Fig. 11, where the reference line, that is, the solid line, represents the ideal estimation results, that is, $Cap_{est} = Cap$. The closer the points approach the reference line, the more accurate the estimation results. Specifically, Cap_{est}s are calculated based on the reference regression functions, which are identified based on the test data of batteries #1 (LFP) and #5 (NCA) in this study. As can be seen, the points in Fig. 11 can overall track the
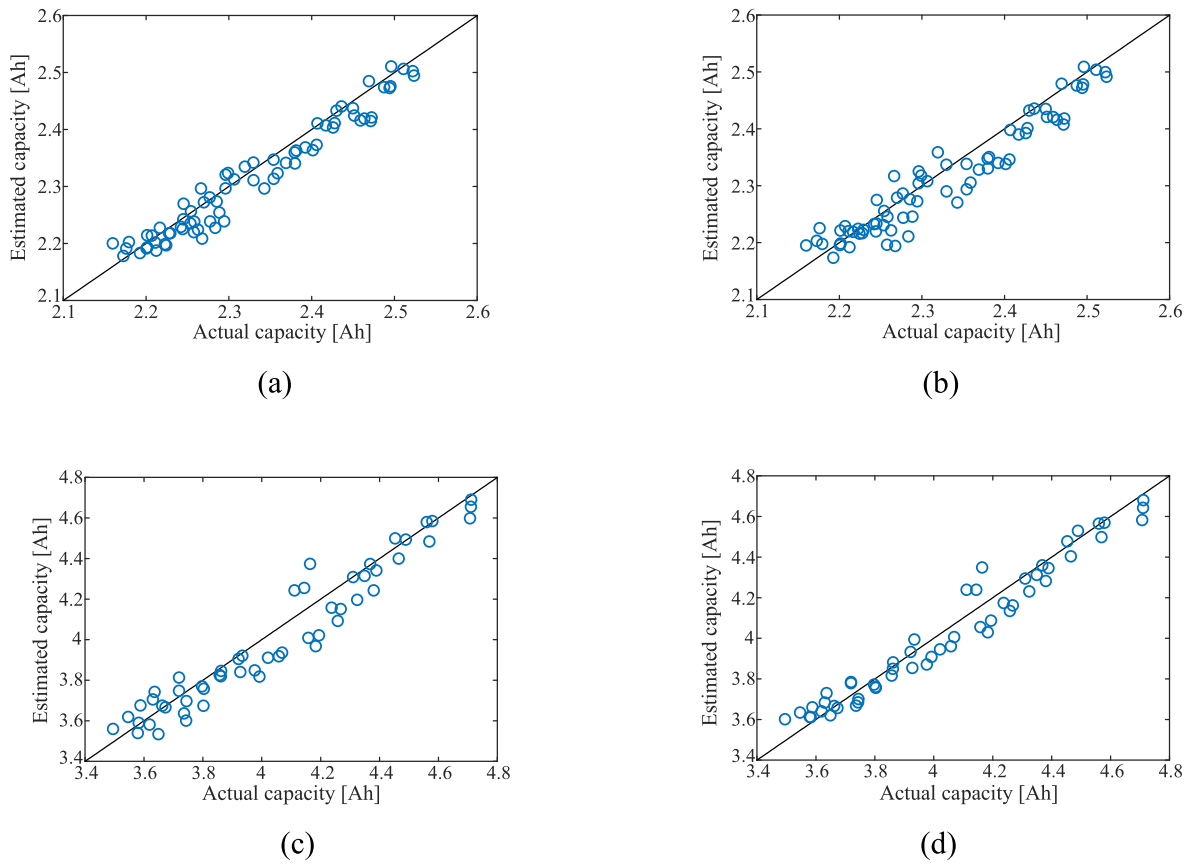
Fig. 13. Estimation results of two batteries with different T_{CV}s. LFP battery with (a) $T_{CV} = 200$ s and (b) $T_{CV} = 1000$ s. NCA battery with (c) $T_{CV} = 2500$ s and (d) $T_{CV} = 3500$ s.
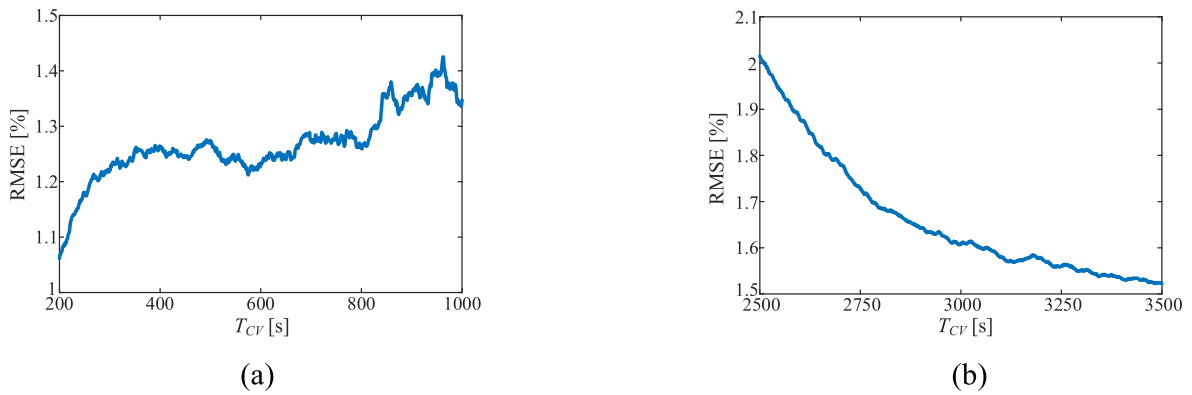
Fig. 14. Evolution of RMSE with respect to T_{CV} for (a) LFP and (b) NCA batteries.

reference line, indicating a satisfactory estimation accuracy for the employed two types of batteries.

In addition, the root-mean-square error (RMSE) between the normalized Cap and Cap_{est}, calculated as (16), is utilized to quantitatively measure the estimation accuracy, where Cap_{nom} denotes the nominal battery capacity,

$$\text{RMSE} = \left[\sqrt{\frac{1}{N_d} \sum_{i=1}^{N_d} \left(Cap_i - Cap_{est,i} \right)^2} \bigg/ Cap_{nom} \right] \times 100\% \qquad (16)$$

The estimation RMSE with respect to different I_{cut}s for the tested batteries are calculated and plotted in Fig. 12. It can be observed that the calculated RMSEs corresponding to the two tested batteries demonstrate the opposite variation trends with respect to I_{cut}, which can be attributed

to the distinct evolution of $|r|$, as shown in Fig. 8. For example, for the LFP battery, the RMSE overall reduces with an increasing I_{cut}. This is mostly due to the fact that T_{CV} at higher I_{cut} demonstrates a stronger correlation with Cap, resulting in a better estimation performance. Even with the varied values, the overall RMSEs for the respective two batteries are less than 1.35% and 2.05% within a certain range of I_{cut}.

B. Case 2: constant T_{CV} cut-off condition

The estimation results under different T_{CV} cut-off conditions for the two tested batteries are exemplarily demonstrated in Fig. 13. As can be seen, for the LFP battery, the estimation results under a lower T_{CV} cut-off condition are much closer to the reference line. While for the NCA battery, the increased cut-off T_{CV} corresponds to a better estimation performance.

The detailed evolution of estimation RMSEs with respect to T_{CV} is
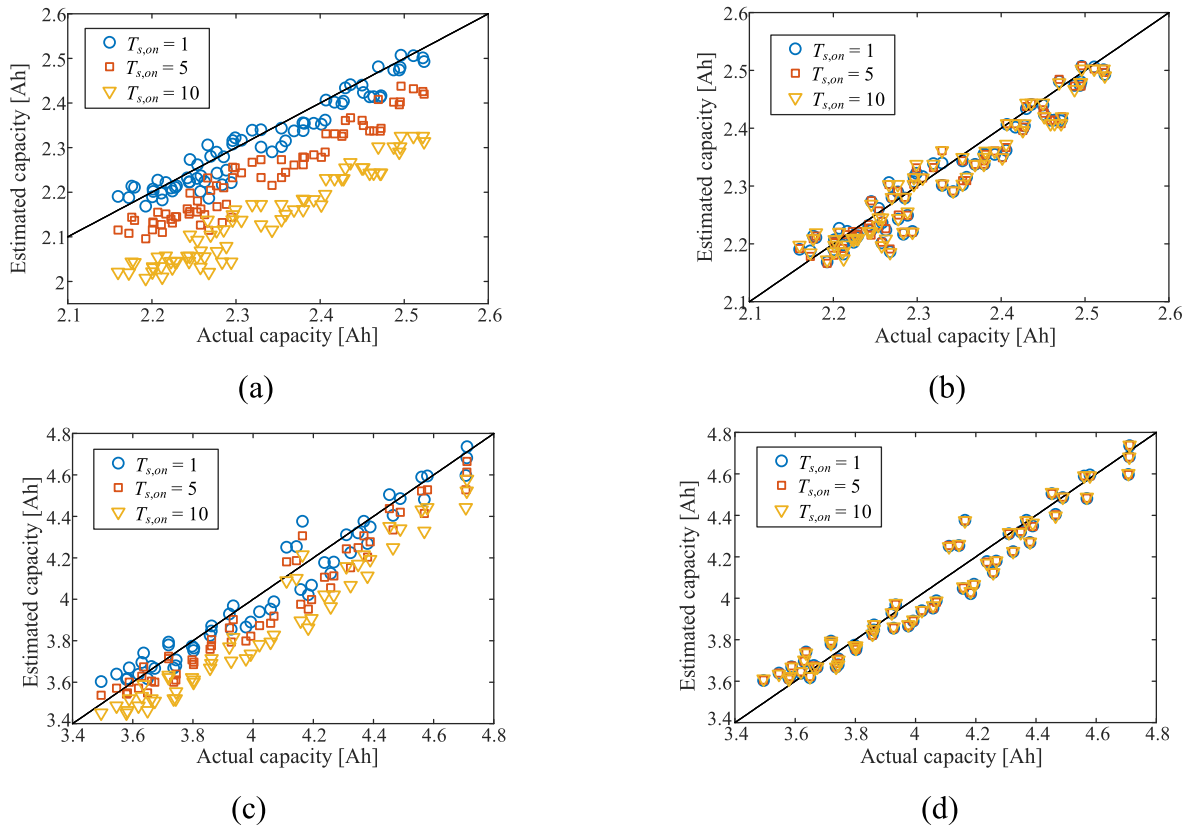
Fig. 15. Estimation results of two batteries with different $T_{s,on}$s. LFP batteries with (a) constant and (b) adaptive buffer lengths. NCA batteries with (c) constant and (b) adaptive buffer lengths.

demonstrated in Fig. 14 to further evaluate the estimation performance. It is clear from Fig. 14 that the RMSEs for the LFP and NCA batteries are generally less than 1.45% and 2.05%, respectively, indicating the feasibility of the proposed method under the constant T_{CV} cut-off condition. In addition, as can be seen, the estimation RMSEs for the LFP and NCA batteries demonstrate the increasing and decreasing variation trends versus T_{CV}, respectively, which are consistent with the estimation results shown in Fig. 13. This is because a larger T_{CV} at a certain aging state corresponding to a lower I_{cut}, suggesting a weaker correlation for the LFP battery and a stronger correlation for the NCA battery, as illustrated in Fig. 8. Therefore, in this case, the estimation accuracy is closely related to the predefined T_{CV}, and the estimation performance may significantly deteriorate when the corresponding I_{cut} is outside the appropriate range.

C. Case 3: different $T_{s,on}$s

To verify the necessity of the T_s-adaptive MAF, the proposed SoH estimation method is implemented based on the test data when $T_{s,on}$s are set as 1, 5, and 10 s. The length of the filter window is set to 30 in this study. The estimation results with constant and adaptive buffer lengths are graphically represented in Fig. 15, where I_{cut}s are set as 0.30 and 0.35 A for the LFP and NCA batteries, respectively. As can be seen, the influence of $T_{s,on}$ on the estimation results is negligible for the proposed method. By contrast, for the method with the constant buffer length, when $T_{s,on}$ is larger than 1 s, the estimated capacities are generally lower than the actual values, as shown in Fig. 15(a) and (c). In addition, the difference between the reference and the actual values is enlarged with the increasing $T_{s,on}$, especially for the employed LFP battery.

The evolution of the estimation RMSE versus I_{cut} is illustrated in Fig. 16 to make a comprehensive investigation.

For the LFP battery, only the results in the range of [0.15 A 0.45 A] are presented for a clear comparison. It can be seen from Fig. 16 that based on the T_s-adaptive MAF, the produced RMSE curves with different

$T_{s,on}$s almost overlap. While for the estimation results with the constant buffer length, the estimation error corresponding to larger $T_{s,on}$ significantly rises as I_{cut} increases. Especially for the LFP battery, the RMSE corresponding to $T_{s,on} = 10$ s is larger than 10% when I_{cut} is set as 0.45 A. In order to illustrate the above phenomena, the measured current and the trajectory of the smoothed current based on different smoothing parameters are exemplarily presented in Fig. 17(a), where $T_{s,off}$ and $T_{s,on}$ are set as 1 and 5 s, respectively. Specifically, curves #1 and #2 represent the smoothed current trajectories based on the adaptive and constant buffer length, that is, $N_{b,on,1} = 6$ and $N_{on,2} = 30$. It can be observed from Fig. 17(a) that curve #1 can track the measured trajectory. By comparison, curve #2 overall lags curve #1, which is consistent with the analysis in Section 3. This means that for a specific I_{cut}, T_{CV} extracted from curve #2 is larger than that extracted from curve #1, leading to the battery capacity estimation lower than the actual value, as illustrated in Fig. 17(b). It should be noted that the difference between $T_{CV,1}$ and $T_{CV,2}$ is enlarged in the high I_{cut} region. This causes the rising RMSE with the increasing I_{cut} under the constant buffer length scenario, as shown in Fig. 16(a) and (c).

5.4. Comparison with conventional T_{CV}-based method

In this section, the conventional T_{CV}-based method is conducted for a comparative study. Since the current is recorded by the high-precision sensor in the laboratory environment, the additional random noise with a standard deviation of 10 mA is added on the measured current to simulate the measurement noise. The capacity estimation results by the conventional and the proposed T_{CV}-based methods are plotted in Fig. 18, and the corresponding RMSEs are listed in Table 3 to make a quantitative comparison.

It can be observed from Fig. 18 that, compared with the proposed method, the conventional method generally produces the results higher
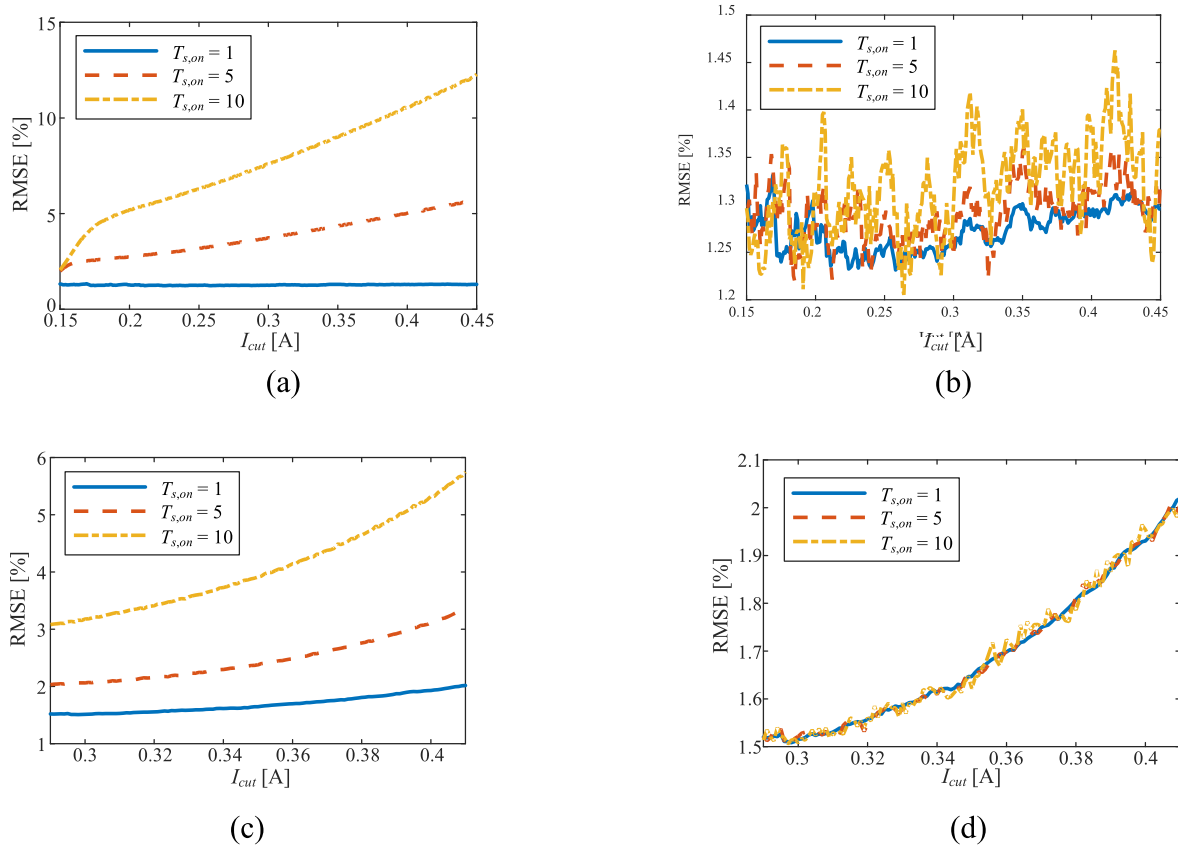
Fig. 16. Evolution of RMSE with respect to I_{cut}. LFP batteries with (a) constant and (b) adaptive buffer lengths. NCA batteries with (c) constant and (d) adaptive buffer lengths.
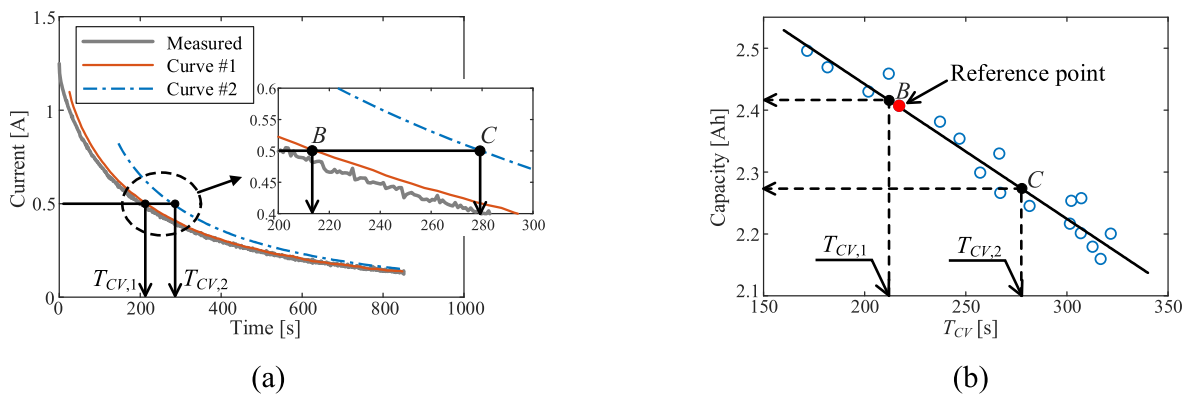

Fig. 17. The illustration of the influence of $T_{s,on}$ on (a) filtered results and (b) capacity estimation results (exemplarily with LFP battery at 96.28% SoH).

than the actual values, leading to larger estimation errors, as shown in Table 3. This is because is affected by the noise disturbance, and the actual CV charging current cannot reach the predefined cutoff value, which resulting in a lower T_{CV} and a higher capacity estimation, in comparison to the actual value. By contrast, the proposed method can update the coefficients of the reference regression function according to the actual I_{cut}. Hence, the produced estimation results are close to the actual values.

5.5. Comparison with different FoIs and offline modeling methods

To further evaluate the performance of the proposed method, three other FoIs proposed in the recent literature and the feedforward neural network (FNN) [45,46] as one of the popular offline modeling methods

are employed to make a comprehensive comparison. The employed FoIs include the time constant of the decoupled CV charging current (τ_{CV}) [36], the energy of the CV charging process (E_{CV}) [38], and the peak area (PA) under the IC curve, i.e., the interval capacity [18,47], during the CC charging process. Specifically, τ_{CV}s are obtained using the dynamic-decoupled parameter identification method based on CV charging data, as reported in our previous work [36]. E_{CV} during each cycle is calculated as [38].

$$E_{CV} = \int_0^{T_{CV}} V_t I(t) dt \qquad (17)$$

where V_t is the battery terminal voltage. For PA, it can be directly obtained from the voltage charging curve under the CC charging scenario, i.e. [18],
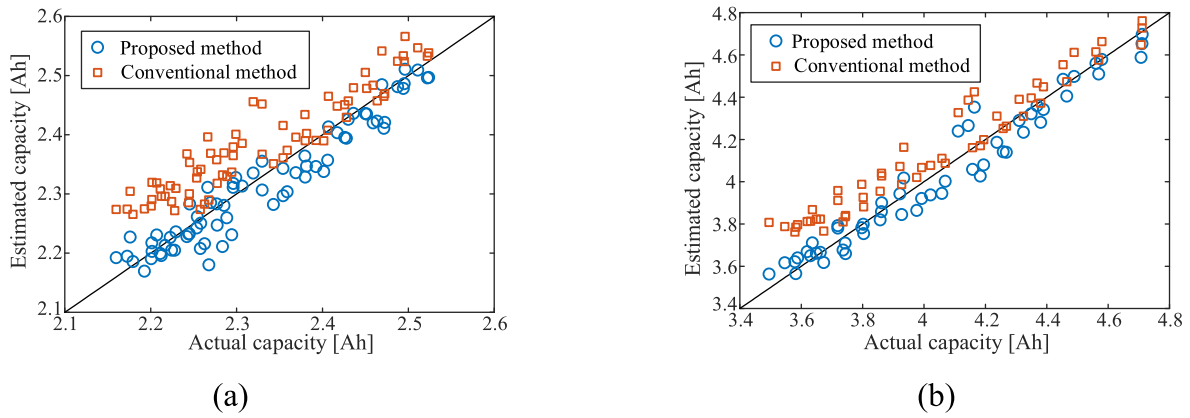
Fig. 18. Comparison of capacity estimation by two methods for (a) LFP and (b) NCA batteries.

Table 3
Comparison of RMSEs based on the proposed and the conventional T_{CV}-based methods.

	LFP		NCA	
	Proposed	Conventional	Proposed	Conventional
RMSE [%]	1.30	2.74	1.56	2.90

$$PA = \int_{V_{low}}^{V_{up}} \frac{dCap}{dV_t} dV_t = Cap(V_{up}) - Cap(V_{low}) = I_{CC}\left[t(V_{up}) - t(V_{low})\right] \quad (18)$$

where I_{CC} denotes the current under the CC charging scenario, V_{low} and V_{up} denote the lower and upper bounds, respectively. The evolutions of the IC curves of the tested LFP and NCA batteries are plotted in Fig. 19. As can be seen, the area under the third peak for the LFP battery, i.e., $Peak_{3,LFP}$, and the area under the second peak for the NCA battery, i.e., $Peak_{2,NCA}$, gradually reduce with the increasing cycle number. Hence, the voltage intervals for the LFP and NCA batteries are selected as [3.38 V, 3.42 V], and [3.67 V, 3.77 V], respectively.

The comparative results of the SoH estimation performance for the LFP and NCA batteries are listed in Tables 4 and 5, respectively, where the required data represent the dataset used for the FoI identification, t_{model} and t_{FoI} represent the computational cost of the offline model construction and the FoI extraction processes, respectively, and both of them are obtained by averaging from 10 runs. The algorithms in this study are implemented on a Lenovo ThinkCentre computer with Intel Core i5-7400 (3-GHz) CPU and 16-GB RAM.

It can be seen from Tables 4 and 5 that all methods can yield the satisfactory estimation results, especially the PA-based method for the

LFP battery and the τ_{CV}-based method for the NCA battery. With respect to the computational cost, due to the two-layer offline modeling process, t_{model} of the proposed T_{CV}-based method is generally longer compared with the τ_{CV}-based method. However, the fitting method consumes less time than the FNN method to establish the offline model. In addition, it can be observed from Tables 4 and 5 that t_{FoI} of T_{CV} is approximately

Table 4
Comparative results of different SoH estimation methods for tested LFP batteries.

FoI	LFP				
	T_{CV}		τ_{CV}	E_{CV}	PA
Modeling method	Fitting	FNN	FNN	FNN	FNN
RMSE [%]	1.32	1.33	1.05	1.42	0.64
t_{model} [s]	0.17	0.68	0.12	0.23	0.25
t_{FoI} [s]	≈ 0	≈ 0	0.08	≈ 0	0.02
Size of required data	Length of N_b		100%	100%	15.43%

Table 5
Comparative results of different SoH estimation methods for tested NCA batteries.

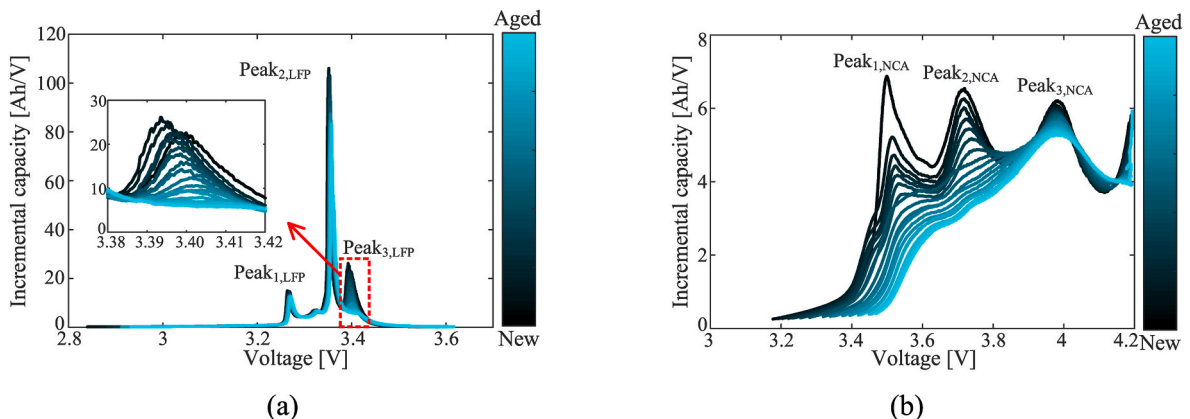| FoI	NCA				
	T_{CV}		τ_{CV}	E_{CV}	PA
Modeling method	Fitting	FNN	FNN	FNN	FNN
RMSE [%]	1.53	1.49	1.47	1.68	1.48
t_{model} [s]	0.26	0.59	0.15	0.32	0.12
t_{FoI} [s]	≈ 0	≈ 0	0.17	≈ 0	0.01
Size of required data	Length of N_b		100%	100%	25.14%

Fig. 19. Evolutions of smoothed IC curves for (a) LFP and (b) NCA batteries.

zero, since it is obtained as soon as the CV charging process is finished. By comparison, the τ_{CV}-based method consumes the most time, which is supposed to be caused by the relatively complex parameter identification process. It is worth noting that although E_{CV} can be immediately acquired when the charge is finished, the integral computation is continuously conducted throughout the CV charging process, as expressed in (17), which means that the entire CV charging data are required. For the PA-based methods, the charging data within the pre-determined voltage interval are required, which are 15.43% and 25.14% of the complete CC charging data for the LFP and NCA batteries, respectively. By contrast, the proposed method only requires the data with the length of N_b at the end of the CV charging process, indicating the lowest storage consumption. In summary, the proposed method shows an overall satisfactory performance comprehensively considering the estimation accuracy, computational cost, and storage consumption.

6. Conclusion

In this paper, we develop an online battery SoH estimation method adaptive to the flexible CV charging profile. The coefficients of the conventional T_{CV}-based SoH model are further expressed as the functions of the actual I_{cut}, and a T_s-adaptive MAF is proposed to acquire the accurate I_{cut} in real time. Verification results demonstrate that within the appropriate I_{cut} range, the proposed method guarantees satisfactory capacity estimations with the RMSE within 1.45% and 2.05% for the respective LFP and NCA batteries under different CV charging profiles. Benefited from the adaptive buffer length, the estimation accuracy is almost maintained in the case of different $T_{s,on}$s. In addition, compared with the conventional T_{CV}-based method, the RMSEs of the proposed method are reduced to within 2% for both types of the tested batteries at a certain I_{cut}, considering the noise disturbance, and the comparison among different FoIs and modeling methods further validate the overall superiority of the proposed method in terms of the estimation accuracy, computational cost, as well as storage consumption.

In this paper, the ambient temperature, the charging current in the previous CC process, i.e., the initial value of the CV charging current, and the CV charging voltage are considered as constant throughout the aging process. However, these variables are generally flexible and uncertain in practical applications, such as the fast-charging scenario in real-world EVs, and this will compromise the performance of the established SoH model. Hence, in our future work, the impacts of the aforementioned stress factors will be considered to further improve the robustness of the proposed method.

Credit author statement

Chris Mi: Conceptualization, Methodology, Supervision, Reviewing and Editing; Jufeng Yang: Data curation, Methodology, Writing - Original draft preparation; Xin Li: Investigation; Xiaodong Sun: Validation, Supervision; Yingfeng Cai:, Validation, Supervision.

Declaration of competing interest

The authors declare that they have no known competing financial interests or personal relationships that could have appeared to influence the work reported in this paper.

Data availability

Data will be made available on request.

Acknowledgments

References

[1] Zhang X, Mi C. Vehicle power management: modeling, control and optimization. Springer Science & Business Media; 2011.
[2] Tomaszewska A, Chu Z, Feng X, O'Kane S, Liu X, Chen J, et al. ETransport. ETransportation 2019;1:100011.
[3] Unterrieder C, Zhang C, Lunglmayr M, Priewasser R, Marsili S, Huemer M. Battery state-of-charge estimation using approximate least squares. J Power Sources 2015; 278:274–86.
[4] Hoque MA, Siekkinen M, Koo J, Tarkoma S. Full charge capacity and charging diagnosis of smartphone batteries. IEEE Trans Mobile Comput 2017;16:3042–55.
[5] Wei Z, Zhao J, He H, Ding G, Cui H, Liu L. Future smart battery and management: advanced sensing from external to embedded multi-dimensional measurement. J Power Sources 2021;489:229462.
[6] Chen C, Xiong R, Yang R, Li H. A novel operational data-driven battery open-circuit voltage characterization mining method for large-scale Applications. Green Energy Intelligent Transport 2022:100001.
[7] Xiong R, Li Z, Yang R, Shen W, Ma S, Sun F. Fast self-heating battery with anti-aging awareness for freezing climates application. Appl Energy 2022;324:119762.
[8] Sui X, He S, Vilsen SB, Meng J, Teodorescu R, Stroe D-I. A review of non-probabilistic machine learning-based state of health estimation techniques for Lithium-ion battery. Appl Energy 2021;300:117346.
[9] Shi M, Xu J, Lin C, Mei X. A fast state-of-health estimation method using single linear feature for lithium-ion batteries. Energy 2022:124652.
[10] Shen P, Ouyang M, Lu L, Li J, Feng X. The co-estimation of state of charge, state of health, and state of function for lithium-ion batteries in electric vehicles. IEEE Trans Veh Technol 2017;67:92–103.
[11] Li Y, Xiong B, Vilathgamuwa DM, Wei Z, Xie C, Zou C. Constrained ensemble Kalman filter for distributed electrochemical state estimation of lithium-ion batteries. IEEE Trans Ind Inf 2020;17:240–50.
[12] Xiong R, Wang J, Shen W, Tian J, Mu H. Co-estimation of State of charge and capacity for Lithium-ion batteries with multi-stage model fusion method. Engineering 2021;7:1469–82.
[13] You G-w, Park S, Oh D. Real-time state-of-health estimation for electric vehicle batteries: a data-driven approach. Appl Energy 2016;176:92–103.
[14] Deng Z, Hu X, Lin X, Xu L, Che Y, Hu L. General discharge voltage information enabled health evaluation for lithium-ion batteries. In: IEEE/ASME Transactions Mechatronics; 2020.
[15] Che Y, Deng Z, Li P, Tang X, Khosravinia K, Lin X, et al. State of health prognostics for series battery packs: a universal deep learning method. Energy 2022;238: 121857.
[16] Li Y, Liu K, Foley AM, Zülke A, Berecibar M, Nanini-Maury E, et al. Data-driven health estimation and lifetime prediction of lithium-ion batteries: a review. Renew Sustain Energy Rev 2019;113:109254.
[17] Stroe D-I, Schaltz E. Lithium-ion battery state-of-health estimation using the incremental capacity analysis technique. IEEE Trans Ind Appl 2019;56:678–85.
[18] Agudelo BO, Zamboni W, Monmasson E. Application domain extension of incremental capacity-based battery SoH indicators. Energy 2021:121224.
[19] Zheng L, Zhu J, Lu DD-C, Wang G, He T. Incremental capacity analysis and differential voltage analysis based state of charge and capacity estimation for lithium-ion batteries. Energy 2018;150:759–69.
[20] Mohtat P, Lee S, Siegel JB, Stefanopoulou AG. Comparison of expansion and voltage differential indicators for battery capacity fade. J Power Sources 2022;518: 230714.
[21] Wu B, Yufit V, Merla Y, Martinez-Botas RF, Brandon NP, Offer GJ. Differential thermal voltammetry for tracking of degradation in lithium-ion batteries. J Power Sources 2015;273:495–501.
[22] Yang J, Cai Y, Mi C. Lithium-ion battery capacity estimation based on battery surface temperature change under constant-current charge scenario. Energy 2022; 241:122879.
[23] Xiong R, Li L, Tian J. Towards a smarter battery management system: a critical review on battery state of health monitoring methods. J Power Sources 2018;405: 18–29.
[24] Tian J, Xiong R, Shen W, Lu J, Yang X-G. Deep neural network battery charging curve prediction using 30 points collected in 10 min. Joule 2021;5:1521–34.
[25] Fly A, Chen R. Rate dependency of incremental capacity analysis (dQ/dV) as a diagnostic tool for lithium-ion batteries. J Energy Storage 2020;29:101329.
[26] Hu X, Che Y, Lin X, Deng Z. Health prognosis for electric vehicle battery packs: a data-driven approach. IEEE/ASME Trans Mechatron 2020;25:2622–32.
[27] Che Y, Deng Z, Lin X, Hu L, Hu X. Predictive battery health management with transfer learning and online model correction. IEEE Trans Veh Technol 2021;70: 1269–77.
[28] Chen Z, Shen W, Chen L, Wang S. Adaptive online capacity prediction based on transfer learning for fast charging lithium-ion batteries. Energy 2022;248:123537.
[29] Wang H, Frisco S, Gottlieb E, Yuan R, Whitacre JF. Capacity degradation in commercial Li-ion cells: the effects of charge protocol and temperature. J Power Sources 2019;426:67–73.
[30] Xie W, Liu X, He R, Li Y, Gao X, Li X, et al. Challenges and opportunities toward fast-charging of lithium-ion batteries. J Energy Storage 2020;32:101837.
[31] Eddahech A, Briat O, Vinassa J-M. Determination of lithium-ion battery state-of-health based on constant-voltage charge phase. J Power Sources 2014;258:218–27.

[32] Williard N, He W, Osterman M, Pecht M. Comparative analysis of features for determining state of health in lithium-ion batteries. Int J Prognostics Health Manag 2013;4.

[33] Liu H, Naqvi IH, Li F, Liu C, Shafiei N, Li Y, et al. An analytical model for the CC-CV charge of Li-ion batteries with application to degradation analysis. J Energy Storage 2020;29:101342.

[34] Ruan H, He H, Wei Z, Quan Z, Li Y. State of health estimation of lithium-ion battery based on constant-voltage charging reconstruction. IEEE J Emeg and Sel Top Power Electron 2021. https://doi.org/10.1109/JESTPE.2021.3098836.

[35] Yang J, Xia B, Huang W, Fu Y, Mi C. Online state-of-health estimation for lithium-ion batteries using constant-voltage charging current analysis. Appl Energy 2018; 212:1589–600.

[36] Yang J, Cai Y, Mi CC. State-of-health estimation for lithium-ion batteries based on decoupled dynamic characteristic of constant-voltage charging current. In: IEEE Transa Transport Electrification; 2021.

[37] Cai L, Lin J, Liao X. An estimation model for state of health of lithium-ion batteries using energy-based features. J Energy Storage 2022;46:103846.

[38] Gong D, Gao Y, Kou Y, Wang Y. State of health estimation for lithium-ion battery based on energy features. Energy 2022;257:124812.

[39] Anseán D, González M, Viera J, García V, Blanco C, Valledor M. Fast charging technique for high power lithium iron phosphate batteries: a cycle life analysis. J Power Sources 2013;239:9–15.

[40] Zheng Y, Ouyang M, Li X, Lu L, Li J, Zhou L, et al. Recording frequency optimization for massive battery data storage in battery management systems. Appl Energy 2016;183:380–9.

[41] Yang J, Cai Y, Pan C, Mi C. A novel resistor-inductor network-based equivalent circuit model of lithium-ion batteries under constant-voltage charging condition. Appl Energy 2019;254:113726.

[42] Ramadass P, Haran B, Gomadam PM, White R, Popov BN. Development of first principles capacity fade model for Li-ion cells. J Electrochem Soc 2004;151:A196.

[43] Smith S. Digital signal processing: a practical guide for engineers and scientists. Elsevier; 2013.

[44] Golestan S, Ramezani M, Guerrero JM, Freijedo FD, Monfared M. Moving average filter based phase-locked loops: performance analysis and design guidelines. IEEE Trans Power Electron 2013;29:2750–63.

[45] Li AG, Wang W, West AC, Preindl M. Health and performance diagnostics in Li-ion batteries with pulse-injection-aided machine learning. Appl Energy 2022;315: 119005.

[46] Sun X, Chen Q, Zheng L, Yang J. Joint estimation of state-of-health and state-of-charge for lithium-ion battery based on electrochemical model optimized by neural network. IEEE J Emerg Sel Top 2022:1.

[47] Li R, Hong J, Zhang H, Chen X. Data-driven battery state of health estimation based on interval capacity for real-world electric vehicles. Energy 2022;257:124771.